

**Observation of ferromagnetic ordering in a stable  $\alpha$ -Co(OH)<sub>2</sub> phase grown on a MoS<sub>2</sub> surface**

Anup Debnath, Shatabda Bhattacharya, and Shyamal K. Saha\*

*Department of Materials Science, Indian Association for the Cultivation of Science, Jadavpur, Kolkata 700032, India*

(Received 1 September 2017; revised manuscript received 30 November 2017; published 26 December 2017)

Because of the potential application of Co(OH)<sub>2</sub> in a magnetic cooling system as a result of its superior magnetocaloric effect many people have investigated magnetic properties of Co(OH)<sub>2</sub>. Unfortunately, most of the works have been carried out on the  $\beta$ -Co(OH)<sub>2</sub> phase due to the fact that the  $\alpha$ -Co(OH)<sub>2</sub> phase is very unstable and continuously transformed into the stable  $\beta$ -Co(OH)<sub>2</sub> phase. However, in the present work, using a MoS<sub>2</sub> sheet as a two-dimensional template, we have been able to synthesize a stable  $\alpha$ -Co(OH)<sub>2</sub> phase in addition to a  $\beta$ -Co(OH)<sub>2</sub> phase by varying the layer thickness. It is seen that for thinner samples the  $\beta$  phase, while for thicker samples  $\alpha$  phase, is grown on the MoS<sub>2</sub> surface. Magnetic measurements are carried out for the samples over the temperature range from 2 to 300 K and it is seen that for the  $\beta$  phase, ferromagnetic ordering with fairly large coercivity (1271 Oe) at 2 K is obtained instead of the usual antiferromagnetism. The most interesting result is the observation of ferromagnetic ordering with a transition temperature (Curie temperature) more than 100 K in the  $\alpha$ -Co(OH)<sub>2</sub> phase. Complete saturation in the hysteresis curve under application of very low field having coercivity of  $\sim$ 162 Oe at 2 K and 60 Oe at 50 K is obtained. A thin stable  $\alpha$ -Co(OH)<sub>2</sub> phase grown on MoS<sub>2</sub> surface with very soft ferromagnetic ordering will be very useful as the core material in electromagnets.

DOI: [10.1103/PhysRevB.96.214433](https://doi.org/10.1103/PhysRevB.96.214433)**I. INTRODUCTION**

It is well known that transition-metal hydroxides exhibit interesting and unusual magnetic behavior [1–5]. In particular, Co(OH)<sub>2</sub> is formed to be very useful in magnetic cooling systems because of its superior magnetocaloric effect (MCE) [6,7]. In general, Co(OH)<sub>2</sub> is crystallized into a hexagonal layered type structure with two polymorphs  $\alpha$ -Co(OH)<sub>2</sub> and  $\beta$ -Co(OH)<sub>2</sub>, in which  $\beta$ -Co(OH)<sub>2</sub> possesses a brucitelike structure with  $a = 3.1$  Å,  $c = 4.6$  Å, and the octahedral with divalent Co contains sixfold coordinated by hydroxyl ions share edges to produce two-dimensional (2D) charge neutral layers stacked one over the other along the  $c$  axis. However,  $\alpha$ -Co(OH)<sub>2</sub> consists of slightly positively charged layers with intercalated charge balancing anions (CH<sub>3</sub>COO<sup>−</sup>, Cl<sup>−</sup>, CO<sub>3</sub><sup>2−</sup>, and NO<sub>3</sub><sup>−</sup>, etc.), [8–10] to restore the charge neutrality. As a result, in the case of  $\alpha$ -Co(OH)<sub>2</sub>, interlayer separation increases substantially and can have a value 7–27 Å according to the size of charge balancing anions. Therefore, with this marked change in lattice spacing of the  $c$  axis and critical interface chemistry, the magnetic property changes drastically in the two structures of  $\alpha$  and  $\beta$  phases.

Out of two phases,  $\beta$ -Co(OH)<sub>2</sub> is stable, however, the  $\alpha$ -Co(OH)<sub>2</sub> phase is metastable and after formation, the  $\alpha$  phase is transformed continuously to a  $\beta$  phase [8,9]. As far as magnetism is concerned, the  $\beta$  phase is known to be an antiferromagnetic [6,7,11–15] in nature but the interlayer interaction diminishes with an increase in interlayer separation as in the case of the  $\alpha$  phase [1,15]. So far many reports on magnetism in Co(OH)<sub>2</sub> are available in the literature but most of them are on the  $\beta$  phase where its magnetic and magnetocaloric effects are concerned. They investigated the phase transition in  $\beta$ -Co(OH)<sub>2</sub> from the antiferromagnetic to weak ferromagnetic state with application of external magnetic field at low temperature [6,7,13,14]. Also the magnetocaloric

effect associated with magnetic phase transition has been reported [6,7]. In this case we are able to grow the ultrathin  $\beta$ -Co(OH)<sub>2</sub> phase on the MoS<sub>2</sub> surface, which shows complete ferromagnetic behavior with high coercivity. By varying the thickness of the  $\beta$ -Co(OH)<sub>2</sub> phase on the MoS<sub>2</sub> surface, we are able to tailor its magnetic saturation at low concentration. Till now all the  $\alpha$ -Co(OH)<sub>2</sub> phase synthesized are poorly crystalline in nature and have a turbostratical disorder along the  $c$  axis where the layers are randomly oriented [8–11]. This prevents creation of a stable  $\alpha$ -Co(OH)<sub>2</sub> phase. Because of an unstable  $\alpha$  phase, magnetic results in  $\alpha$ -Co(OH)<sub>2</sub> have not yet been reported. Therefore, to synthesize stable  $\alpha$ -Co(OH)<sub>2</sub> on the MoS<sub>2</sub> surface to investigate its magnetic properties is a real challenge. In the previous works [16–18] we have reported many interesting magnetic results on transition metals and their hydroxides grown on graphene and MoS<sub>2</sub> surfaces. Exploiting the interface interaction, in the present work, we have been able to synthesize a stable  $\alpha$ -Co(OH)<sub>2</sub> phase considering MoS<sub>2</sub> as a two-dimensional template. The thickness has been controlled by changing the concentration of the Co precursor. We have prepared four samples with different concentrations of Co precursor keeping the MoS<sub>2</sub> concentration constant. It is seen that for lower concentrations the  $\beta$ -Co(OH)<sub>2</sub> phase is grown while for higher concentrations the  $\alpha$ -Co(OH)<sub>2</sub> phase is grown. The most interesting result is the synthesis of stable  $\alpha$ -Co(OH)<sub>2</sub> layers using the MoS<sub>2</sub> sheet as a 2D template. The magnetic measurements are carried out on all the samples over the temperature from 2 to 300 K. Because of charge transfer [16] from S to Co the usual antiferromagnetic nature has not been obtained in the case of a thin layered  $\beta$ -Co(OH)<sub>2</sub> phase grown on the MoS<sub>2</sub> surface; rather perfect ferromagnetic ordering with fairly large coercivity of 1271 Oe is observed in this case.

As the  $\alpha$ -Co(OH)<sub>2</sub> phase grown on the MoS<sub>2</sub> sheet is very stable for a higher concentration of Co precursor, we have been able to investigate the detailed magnetic properties in this thin layered  $\alpha$ -Co(OH)<sub>2</sub> sample. Perfect ferromagnetic saturation under very low magnetic field (<1000 Oe) with coercivity of

\*cnssks@iacs.res.in

~162 Oe at 2 K is observed. The coercivity as usual changes with increasing temperature. It is to be mentioned that the as-grown stable  $\alpha$ -Co(OH)<sub>2</sub> phase shows soft ferromagnetism with very low coercivity which will be very useful as the core material in an electromagnet.

## II. EXPERIMENTAL SECTION

### A. Synthesis

For preparation of samples, ammonium molybdate tetrahydrate [(NH<sub>4</sub>)<sub>6</sub>Mo<sub>7</sub>O<sub>24</sub>·4H<sub>2</sub>O] (81.0–83.0%), thiourea [(NH<sub>2</sub>)<sub>2</sub>CS] (99.0%), and cobalt (II) acetate [Co(CH<sub>3</sub>COO)<sub>2</sub>] were purchased from Sigma-Aldrich. In the first step, we prepared the MoS<sub>2</sub> sheet using a technique reported elsewhere [16]. In the second step, 50 mg of as-prepared MoS<sub>2</sub> was dispersed in 100 ml of DMF (N,N-dimethyl formamide) taken in a 250-ml beaker followed by ultrasonic vibration for 2.5 h. The resulting dispersion was stirred in a magnetic stirrer at a constant temperature at 80° C. In another beaker, an aqueous solution of cobalt acetate was prepared at room temperature. Then the cobalt acetate solution was added drop by drop within the dispersed MoS<sub>2</sub> in DMF at a temperature of 80° C under constant stirring. The reaction continued to 1 h at a constant temperature of 80° C under stirring conditions. The reaction precipitation was collected and washed several times by deionized water and finally a hydrothermal reaction was carried out within a Teflon lined stainless-steel autoclave for 24 h at a temperature of 200° C. The final product was washed by deionized water followed by acetone and alcohol and the product was dried at 60° C for 6 h. We prepared four different samples of Co(OH)<sub>2</sub>/MoS<sub>2</sub> composite by varying the concentration of Co(OH)<sub>2</sub> precursor designated as S6, S12, S18, S30 for the 6, 12, 18, and 30 mg of cobalt precursor (i.e., cobalt acetate) respectively for a constant amount (50 mg) of MoS<sub>2</sub>.

### B. Characterization

For characterization of the as-prepared samples, we performed powder x-ray diffraction (XRD) using a Bruker D8 advance diffractometer, Da Vinci model. Fourier transform infrared (FTIR) spectroscopic measurement was carried out using a Nicolet Magna IR 750 system. UV-VIS absorption spectra were measured using a Cary UV 5000 spectrophotometer. Atomic force microscopy (AFM) measurement was done using the Asylum Research MFP-3D Origin system. Raman spectroscopy measurement was carried out by a JYT6400 micro-Raman spectrophotometer. X-ray photoelectron spectroscopy (XPS) was investigated by a OMICRON-0571 system. Transmission electron microscopy (TEM) measurement was studied by a JEOL-2011 high-resolution transmission electron microscope. For magnetic measurements we have used a superconducting quantum interference device magnetometer, Quantum Design MPMS XL 5.

#### 1. X-ray diffraction and Rietveld refinement

Structural (lattice parameters) and microstructural (particle size and rms lattice strain) characterization of the as-prepared samples were done by using Rietveld refinement analysis [19] of the powder x-ray diffraction (XRD) pattern using MAUD 2.5.5

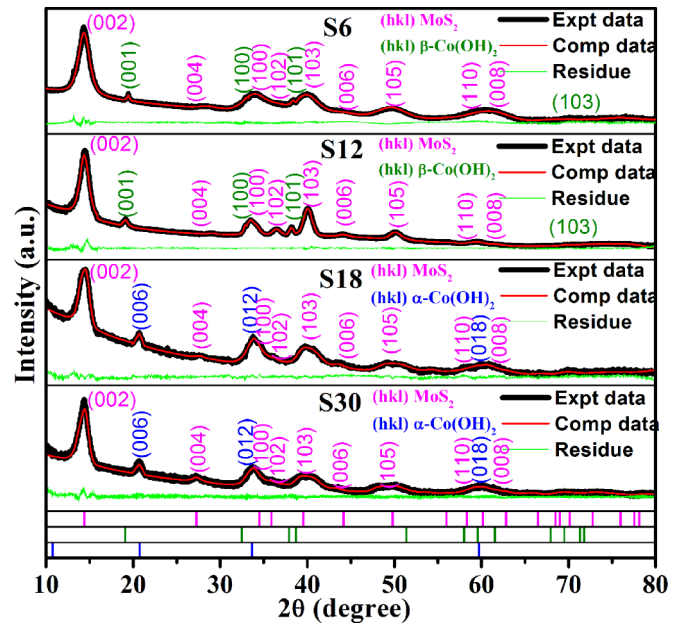


FIG. 1. XRD-Rietveld refinement patterns of samples S6, S12, S18, and S30. Black lines represent experimental curve, red lines are fitted curves, the green lines represent the residue (subtracted value of experimental and theoretical data), and the vertical line “|” at the very bottom represents the theoretical Bragg positions for all the phases present [purple is for MoS<sub>2</sub>, green is for  $\beta$ -Co(OH)<sub>2</sub>, and blue is for  $\alpha$ -Co(OH)<sub>2</sub>].

version software [20]. Powder XRD profiles of all samples shown in Fig. 1 were taken from 10° to 80° with a step size of 0.02° at a scan rate of 5 sec/step. The wavelength of the x ray used was 1.54 Å (Cu K<sub>α</sub> line). For fitting the observed data with the calculated data we used here the Marquardt least-squares refinement procedure. For estimating the crystalline size and lattice strain of all samples we used here the pseudo-Voigt profile fitting function. The quality of fitting was determined by using the well-known formula with goodness of fitting (GOF)  $GOF = \frac{R_{wp}}{R_{exp}}$ , where  $R_{wp}$  and  $R_{exp}$  are the weighted residual error and the expected error respectively and are defined as  $R_{wp} = [\frac{\sum_i w_i (I_o - I_c)^2}{\sum_i w_i (I_o)^2}]^{1/2}$ ,  $R_{exp} = [\frac{(N-P)}{\sum_i w_i (I_o)^2}]^{1/2}$ , where  $I_o$  and  $I_c$  are the experimental and calculated data respectively,  $w_i$  is the weight,  $N$  is the number of experimental observations, and  $P$  is the number of fitting parameters. All parameters have been refined until convergence of the quality factor, i.e., the value of GOF becomes very close to 1.0.

From the XRD data, it is seen that for lower concentration of the Co precursor (samples S6 and S12) the  $\beta$ -Co(OH)<sub>2</sub> phase is formed. However, for higher concentration (samples S18 and S30), the  $\alpha$ -Co(OH)<sub>2</sub> phase is formed on the MoS<sub>2</sub> surface. The volume fractions of MoS<sub>2</sub> and  $\beta$ -Co(OH)<sub>2</sub> for samples S6 and S12 have been estimated from Rietveld analysis as 99.66%, 0.34% and 96.09%, 3.91% respectively. However, for samples S18 and S30, the volume fraction of MoS<sub>2</sub> and  $\alpha$ -Co(OH)<sub>2</sub> phases have been estimated as 51.41%, 48.59% and 50.51%, 49.49% respectively. It is also noticed in the XRD data that the  $\alpha$ -Co(OH)<sub>2</sub> phase shows much stronger peaks compared to the  $\beta$ -Co(OH)<sub>2</sub> phase because of higher thickness with a

TABLE I. Different structural and microstructural parameters obtained from Rietveld analysis of  $\text{Co(OH)}_2/\text{MoS}_2$  composites for two different polymorphs of  $\text{Co(OH)}_2$ .

Sample	Crystalline phases	Volume fraction (%)	Cell length (Å)		Particle size (nm)	Lattice strain ( $\times 10^{-6}$ )	GOF
			a	c			
S6	$\text{MoS}_2$	$99.66 \pm 0.81$	$3.121 \pm 0.001$	$12.633 \pm 0.011$	$108.07 \pm 0.01$	$9.82 \pm 0.01$	1.08
	$\beta\text{-Co(OH)}_2$	$0.34 \pm 0.07$	$3.173 \pm 0.001$	$4.640 \pm 0.001$	$10.49 \pm 0.11$	$6.20 \pm 0.03$	
S12	$\text{MoS}_2$	$96.09 \pm 0.49$	$3.116 \pm 0.001$	$12.351 \pm 0.001$	$97.15 \pm 0.01$	$7.39 \pm 0.01$	1.59
	$\beta\text{-Co(OH)}_2$	$3.91 \pm 0.01$	$3.143 \pm 0.001$	$4.822 \pm 0.001$	$9.61 \pm 0.01$	$9.56 \pm 0.01$	
S18	$\text{MoS}_2$	$51.41 \pm 0.84$	$3.095 \pm 0.001$	$12.441 \pm 0.004$	$129.34 \pm 3.75$	$8.30 \pm 0.03$	1.15
	$\alpha\text{-Co(OH)}_2$	$48.59 \pm 0.01$	$3.148 \pm 0.010$	$26.108 \pm 0.016$	$12.14 \pm 2.25$	$4.92 \pm 0.04$	
S30	$\text{MoS}_2$	$50.51 \pm 0.93$	$3.101 \pm 0.001$	$12.638 \pm 0.016$	$106.98 \pm 2.77$	$5.34 \pm 0.04$	1.32
	$\alpha\text{-Co(OH)}_2$	$49.49 \pm 0.01$	$3.170 \pm 0.002$	$26.453 \pm 0.030$	$9.14 \pm 2.37$	$3.27 \pm 0.01$	

larger number of layers. As obtained from the analysis the crystal structure symmetry of the  $\text{MoS}_2$  phase is hexagonal and the space group is  $P6_3/mmc$ . All the parameters obtained from Rietveld analysis are summarized in Table I. For fitting the XRD data we have used ICSD database nos. 1010993 and 1010267 and JCPDS card no. 37-1492 and 51-1731 [21].

### 2. Fourier transform infrared spectroscopy measurement

To distinguish between  $\alpha$  and  $\beta$  phases and to understand the structural configuration of the as-prepared samples we have performed Fourier transform infrared (FTIR) spectroscopy measurement. From the FTIR spectra as shown in Fig. 2(a), it is seen that there are several characteristic signatures of the different functional groups present in the samples. The broad spectra between  $3322$  and  $2680 \text{ cm}^{-1}$  correspond to O-H stretching vibration which is present in the case of all samples. In the region near  $1401$  and  $968 \text{ cm}^{-1}$  there are two dips which correspond to the O-H bending mode and are also present in all the samples. The Co-OH stretching vibration mode has been identified near  $648 \text{ cm}^{-1}$  and the Mo-S stretching vibration mode appears around  $476 \text{ cm}^{-1}$  [22]. In the case of samples S18 and S30, there are two additional dips near  $1712$  and  $1273 \text{ cm}^{-1}$  which correspond to C=O stretching vibration and C-O stretching vibration of the carbonyl group respectively [22,23]. These two additional dips are absent in the case of

samples S6 and S12. The presence of C=O and C-O stretching vibration modes indicates the existence of extra acetate ions in the  $\alpha\text{-Co(OH)}_2$  phase. The excess charge balancing acetate anions are intercalated in between two  $\alpha\text{-Co(OH)}_2$  layers. With this intercalation of extra acetate ions the interlayer separation between two parallel  $\text{Co(OH)}_2$  layers is increased in the case of the  $\alpha$  phase which has also been verified by XRD Rietveld analysis, where the lattice parameter  $c$  along the vertical direction is increased. In the case of samples S6 and S12, the absence of spectra near  $1712$  and  $1273 \text{ cm}^{-1}$  indicates that there are no acetate anions intercalated within the sample which shows a pure  $\beta\text{-Co(OH)}_2$  phase.

### 3. UV-visible spectroscopy measurement

To investigate the presence of  $\text{Co}^{2+}$  in tetrahedral and octahedral configurations to differentiate  $\alpha$  and  $\beta$  phases we have performed UV-visible spectroscopic measurement. In the UV-visible profile as shown in Fig. 2(b), we get several peaks among which the peak positions near  $284$ ,  $330$ ,  $400$ ,  $448$ ,  $618$ , and  $666 \text{ nm}$  correspond to the  $\text{MoS}_2$  phase [24,25], which is present in all samples. The two humps near  $500$  and  $530 \text{ nm}$  correspond to  $\text{Co}^{2+}$  in the octahedral configuration [26] found in samples S12, S18, and S30. However, another two humps near  $590$  and  $640 \text{ nm}$  correspond to  $\text{Co}^{2+}$  in the tetrahedral configuration [26] found only in

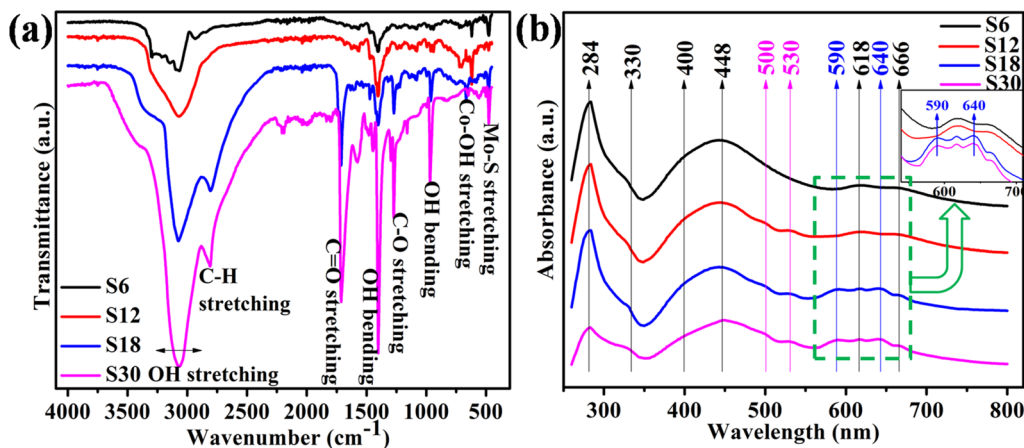


FIG. 2. (a) FTIR transmittance spectra, and (b) UV-vis absorbance spectra of samples S6, S12, S18, and S30.

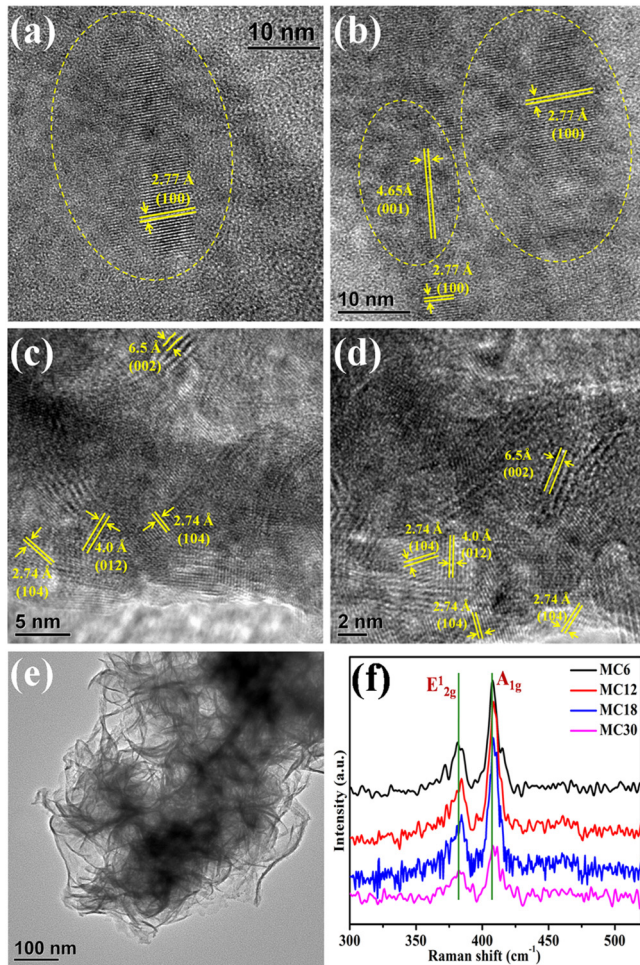


FIG. 3. High-resolution TEM images and the lattice planes of the samples (a) S6, (b) S12, (c) S18, (d) S30, (e) microstructure of composite material, and (f) Raman spectra of MoS<sub>2</sub> samples.

samples S18 and S30. Therefore, S12 has a pure  $\beta$ -Co(OH)<sub>2</sub> phase with octahedral peaks whereas S18 and S30 have both octahedral and tetrahedral peaks because of the presence of the  $\alpha$ -Co(OH)<sub>2</sub> phase. In the case of sample S6 no significant peak or hump is observed due to Co<sup>2+</sup> sites other than the MoS<sub>2</sub> characteristic peaks. The reason behind this is the amount of Co(OH)<sub>2</sub> with respect to MoS<sub>2</sub> is quite low in this case.

#### 4. TEM image analysis

The morphology of the growth structure of the as-prepared samples has been investigated using transmission electron microscopy. In the case of the S6 sample we observed (001) crystal planes with lattice spacing 2.77 Å as shown in Fig. 3(a), which are of  $\beta$ -Co(OH)<sub>2</sub> phase. In the case of the S12 sample we got a (100) plane with crystal lattice spacing of 2.77 Å along with (001) plane with spacing 4.65 Å as shown in Fig. 3(b), which are also of  $\beta$ -Co(OH)<sub>2</sub> phase. In the case of the S18 sample we got a (104) plane with spacing 2.74 Å along with a (012) plane with spacing 4.0 Å as shown in Fig. 3(c), which corresponds to the  $\alpha$ -Co(OH)<sub>2</sub> phase. In the case of the S30 sample we got a (104) plane with spacing 2.74 Å along with a (012) plane with spacing 4.0 Å as shown in Fig. 3(d), which

also corresponds to the  $\alpha$ -Co(OH)<sub>2</sub> phase. In the case of S18 and S30 samples because of overgrowth of the  $\alpha$ -Co(OH)<sub>2</sub> layer, several randomly oriented (104) and (012) planes are observed, as shown in Figs. 3(c) and 3(d). This (012) plane is also observed in the XRD profile and hence confirms the presence of the  $\alpha$ -Co(OH)<sub>2</sub> phase. The MoS<sub>2</sub> sheet used as a template was in the mesoscopic scale, though it is very difficult to understand the dimension of a single sheet as sheets overlap each other and form a continuous sheet.

#### 5. Thickness measurement by AFM and Raman analysis

The thickness of the Co(OH)<sub>2</sub> layer grown on the MoS<sub>2</sub> surface has been measured by atomic force microscopy (AFM). In the case of the S30 sample, the average thickness of Co(OH)<sub>2</sub> layers grown on the MoS<sub>2</sub> surface is found to be about 14 nm as shown in Fig. 4(a). In the case of the S18 sample, the thickness is obtained as 8.87 nm as shown in Fig. 4(b). For  $\alpha$  phases, i.e., for S30 and S18 samples, Co(OH)<sub>2</sub> has larger interlayer separation and consequently larger thickness, because of the intercalated charge balancing anions present between the layers. However for  $\beta$  phases (samples S6 and S12) the average height is very small compared to  $\alpha$  phases as shown in Figs. 4(c) and 4(d). For the S12 sample, the average height is 3.31 nm as found from AFM analysis. While for the S6 sample, there are only a few layers of Co(OH)<sub>2</sub> and the thickness is very small (1.55 nm) as shown in Fig. 4(d). So from AFM analysis we can estimate the thickness of the phases of Co(OH)<sub>2</sub> grown on the MoS<sub>2</sub> surface and they vary with the change in concentration of the Co precursor.

To find the layer thickness of MoS<sub>2</sub> we have performed Raman spectroscopy. In the Raman spectra of MoS<sub>2</sub>, the shift of the A<sub>1g</sub> mode occurs as a function of layer number however the E<sub>12g</sub> mode shifts in the opposite direction because of stacking induced structural changes. The bifurcation between A<sub>1g</sub> and E<sub>12g</sub> increases with increase of layer number [27]. In our case, the bifurcation of two modes (A<sub>1g</sub> and E<sub>12g</sub>) starts at about 26.53 cm<sup>-1</sup> which indicates the layer number of MoS<sub>2</sub> is more than 10.

#### 6. X-ray photoelectron spectroscopy measurement

Analyzing the x-ray photoelectron spectroscopy (XPS) profile of a typical sample, we get an estimation of the ionic state of the elements present in the Co(OH)<sub>2</sub>/MoS<sub>2</sub> composite and at the same time we get an idea of charge transfer from the S 2p to Co 3d orbital at the interface. In the overall XPS profile as shown in Fig. 5(a), there are three peaks of Mo at binding energies of 230.7, 395.7, and 413.2 eV which correspond to Mo 3d, 3p<sub>3/2</sub>, and 3p<sub>1/2</sub> orbitals respectively. An intense peak has been observed at 163.2 eV which corresponds to the S 2p of the MoS<sub>2</sub> phase [28] as shown in Fig. 5(f). There are two other intense peaks of binding energies 780.7 and 796.96 eV corresponding to Co 2p<sub>3/2</sub> and 2p<sub>1/2</sub> states of the Co(OH)<sub>2</sub> phase [29] respectively as shown in Fig. 5(b). Another small peak in the low-energy range at 105.7 eV corresponds to the Co 2s orbital. The strong peak at 533.2 eV corresponds to O 1s associated with the OH<sup>-</sup> group of Co(OH)<sub>2</sub> [29] as shown in Fig. 5(c). If minutely observed it can be found that the binding energy of S 2p increases from 162.40 to 163.20 eV as

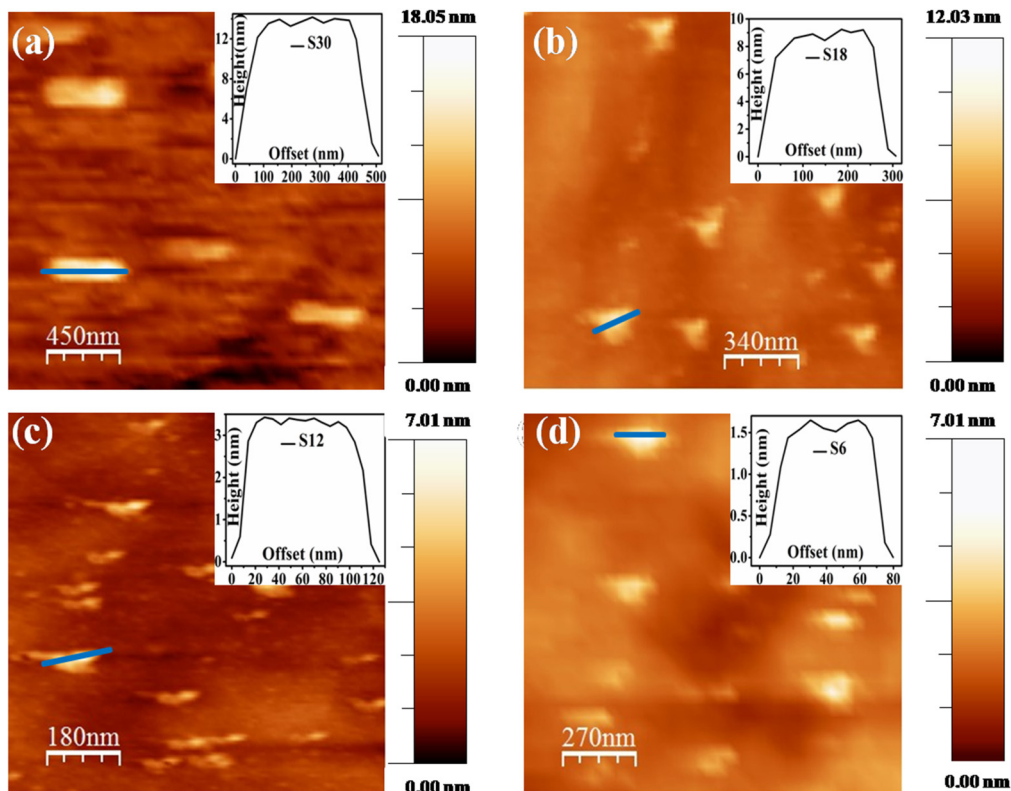


FIG. 4. AFM images with height profiles of the samples (a) S30, (b) S18, (c) S12, and (d) S6.

compared with the literature [28], while that for Co  $2p_{3/2}$  and  $2p_{1/2}$  decrease from 781 to 780.70 eV and 797.80 to 796.96 eV respectively [29]. The change in binding energies obtained from XPS analysis is also tabulated in Table II. From the reference value of the binding energy of S  $2p$  and Co  $3d$  orbital

we get a direct evidence of the change in orbital energies and hence charge transfer from S to Co. The delocalized outermost electrons of the S  $2p$  orbital are partially transferred to Co  $3d$  via “ $d-p$ ” mixing [16,30,31]. We have explain this part elaborately in a later section.

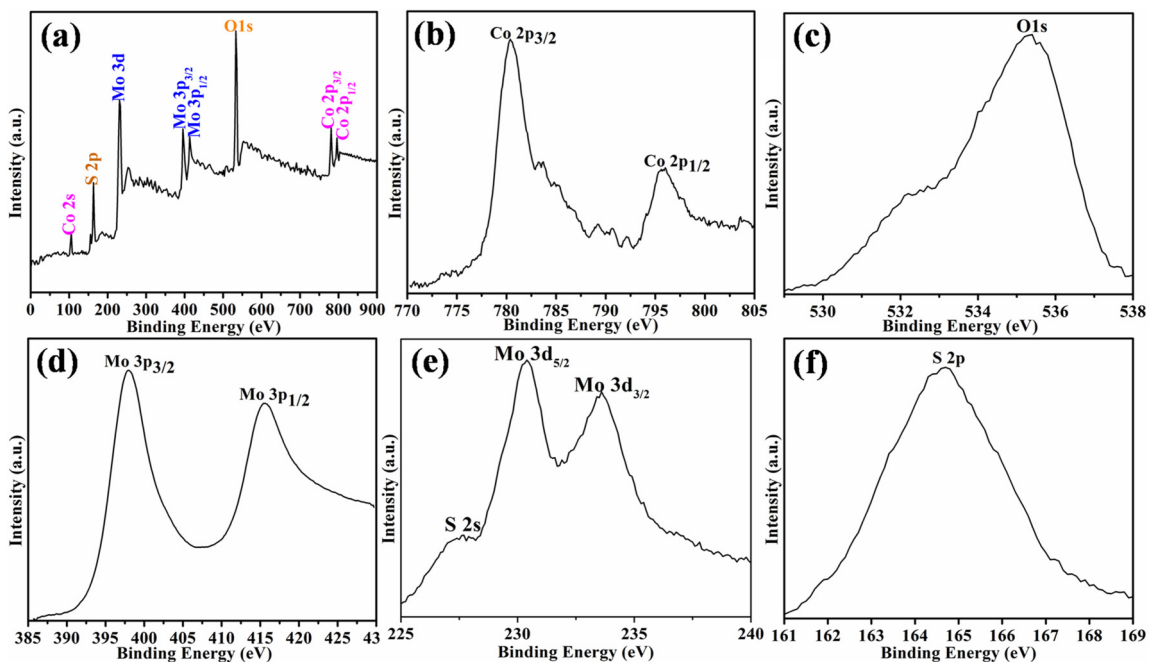


FIG. 5. XPS profile of Co(OH)<sub>2</sub>/MoS<sub>2</sub> (a) in full range view, and (b) high-resolution scan of Co  $2p$  orbital, (c) O  $1s$ , (d) Mo  $3p$ , (e) S  $2s$  and Mo  $3d$ , and (f) S  $2p$  orbital.

TABLE II. Shift in binding energy of orbitals from XPS profile.

Element	Orbitals	Binding energy (eV)		Shift in binding energy (due to charge transfer) (eV)
		Experimental value	Standard value	
S	2p	163.20	162.40	+0.80
Co	2p <sub>3/2</sub>	780.70	781.00	-0.30
	2p <sub>1/2</sub>	796.96	797.80	-0.84

### III. RESULTS AND DISCUSSION

#### A. Structural analysis

For S6 and S12 samples,  $\beta$ -Co(OH)<sub>2</sub> has been formed however for higher concentration, i.e., for S18 and S30 samples we get  $\alpha$ -Co(OH)<sub>2</sub> phase.  $\beta$ -Co(OH)<sub>2</sub> is the stoichiometric phase and has a brucitelike structure in which there are Co<sup>2+</sup> ions octahedrally coordinated with hexagonal packing of hydroxyl ions [8,9], whereas  $\alpha$ -Co(OH)<sub>2</sub> is in a general metastable phase and has a crystal structure of isostructural hydrotalcitelike structure consisting of positively charged Co(OH)<sub>2-x</sub> layers intercalated with different charge balancing anions (e.g., acetate, chlorite, nitrate, carbonate, excess hydroxyl, etc.) [8–11]. In  $\alpha$ -Co(OH)<sub>2</sub>, there are vacant octahedral sites and each vacancy is capped by two tetrahedral coordinated divalent Co<sup>2+</sup> ions on opposite sides of the layer. The positively charged  $\alpha$ -Co(OH)<sub>2</sub> in the form of Co(OH)<sub>2-x</sub> make a charge balance forming a hydrogen bond and/or van der Waals force with excess water or acetate anions intercalated between two layers of Co(OH)<sub>2-x</sub> and stacked together (Fig. 6). In the case of S6 and S12 samples, the amount of cobalt precursor is quite low with respect to the MoS<sub>2</sub>. This is why the charge-neutral layer  $\beta$ -Co(OH)<sub>2</sub> is formed, whereas in the case of the S18 and S30 samples there is a huge amount of cobalt precursor along with acetate ions, which may cause the charge-neutral agent for the formation of  $\alpha$ -Co(OH)<sub>2</sub>.

#### B. Magnetic analysis

##### 1. Magnetic interaction in $\beta$ -Co(OH)<sub>2</sub>/MoS<sub>2</sub> phase

To investigate the magnetic properties of  $\beta$ -Co(OH)<sub>2</sub> and  $\alpha$ -Co(OH)<sub>2</sub> phases grown on a MoS<sub>2</sub> sheet we have carried

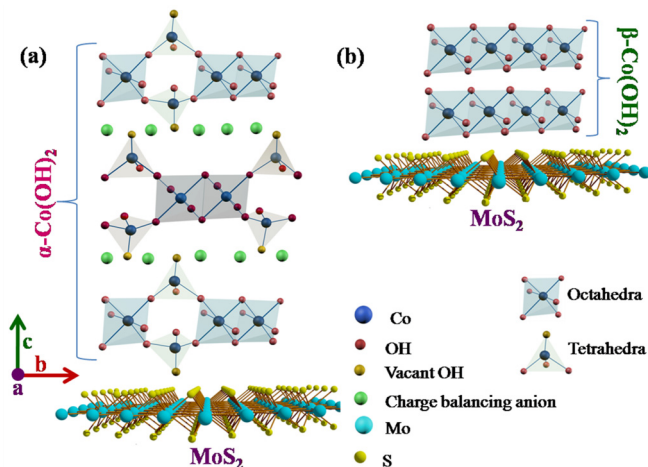


FIG. 6. Schematic diagram of (a)  $\alpha$ -Co(OH)<sub>2</sub>/MoS<sub>2</sub>, and (b)  $\beta$ -Co(OH)<sub>2</sub>/MoS<sub>2</sub> composite. Hydrogen and water molecules are omitted for clarity.

out the magnetic measurements over the temperature range from 2 to 300 K in a fixed magnetic-field strength of 50 Oe. The susceptibility ( $\chi$ ) vs temperature ( $T$ ) curves in zero-field-cooled and field-cooled conditions (ZFC and FC) for the sample S6 are shown in Fig. 7(a). Two peaks are obtained in the ZFC curve. One is near 10.07 K and the other is at 114.2 K. The first one is for the  $\beta$ -Co(OH)<sub>2</sub> phase [6,7,12,13] and the second one is for the defect state of MoS<sub>2</sub>. And there is a paramagnetic tail below 5 K. The magnetic hysteresis (MH) curve for this sample shows a ferromagnetic behavior at the low-temperature regime as shown in Fig. 7(b). Below 5 K, a competition between paramagnetic and ferromagnetic nature is noticed in the MH curve. As a result, perfect saturation is not observed however we have seen a ferromagnetic saturation at 10 K. In case of 20 and 60 K, we have seen a diamagnetic nature because of the high mole percentage of MoS<sub>2</sub> with respect to the  $\beta$ -Co(OH)<sub>2</sub> phase and the magnetic behavior of MoS<sub>2</sub> dominates over the magnetic behavior of  $\beta$ -Co(OH)<sub>2</sub> and as a whole it shows diamagnetic nature.

In the case of the S12 sample, there is only one peak in the ZFC curve near about 10.36 K which is due to the  $\beta$ -Co(OH)<sub>2</sub> phase [6,7,12,13] as shown in Fig. 7(c) and there is also a bifurcation between the ZFC and FC curves which indicates the ferromagnetic behavior with coercivity in the MH loop [Fig. 7(d)]. The MH curve shows ferromagnetic saturation up to 10 K. After the transition temperature at 10.36 K the sample shows paramagnetic behavior. We have fitted the  $1/\chi$  vs  $T$  curve with the Curie-Weiss law  $\frac{1}{\chi} = \frac{T-\Theta}{C}$ , as shown in the inset of Fig. 7(c) and we get the Curie constants  $\Theta = 10.34$  K and  $C = 3.63 \times 10^{-4}$  emu Kg<sup>-1</sup> Oe<sup>-1</sup> (Table IV). For this sample, using the relation  $N = \frac{N_A M}{M_W}$  ( $N_A$  is the Avogadro number,  $M_W$  is the molecular weight, and  $M$  is the total mass of the sample after preparation), the total Co<sup>2+</sup> ions present per gram of the sample  $N$  is obtained as  $1.41 \times 10^{20}$ . For Co<sup>2+</sup>, the  $g$  value is taken as 2.191 [32]. Using the formulas  $C = \frac{N\mu^2}{3k_B}$  and  $\mu^2 = g^2\mu_B^2 S(S+1)$  we get the value of average spin as  $S = 1.17$ . And using the formula  $M_S = Ng\mu_B(S)$  we have calculated the saturation magnetization as  $M_S = 3.38$  emu/g Oe whereas the experimental value obtained from asymptote of the MH curve with  $T \rightarrow 0$  K is  $M_S = 2.52$  emu/g Oe (Table V). In  $\beta$ -Co(OH)<sub>2</sub> Co<sup>2+</sup> situated at the center of each octahedral and each octahedral coordinates each other by the corner O atom and forms an octahedral layer type structure. In each lateral octahedral, all spins are in the same direction but the alternate direction in the interlayer octahedral. As a result, the  $\beta$ -Co(OH)<sub>2</sub> shows the antiferromagnetic coupling in the bulk phase [6,7,12,13]. But when it grows on the MoS<sub>2</sub> sheet then charge transfer [33–37] occurs from sulfur to cobalt resulting in a reduction of spins in the layer of cobalt octahedra adjacent to MoS<sub>2</sub>. This causes a net magnetic moment in the case

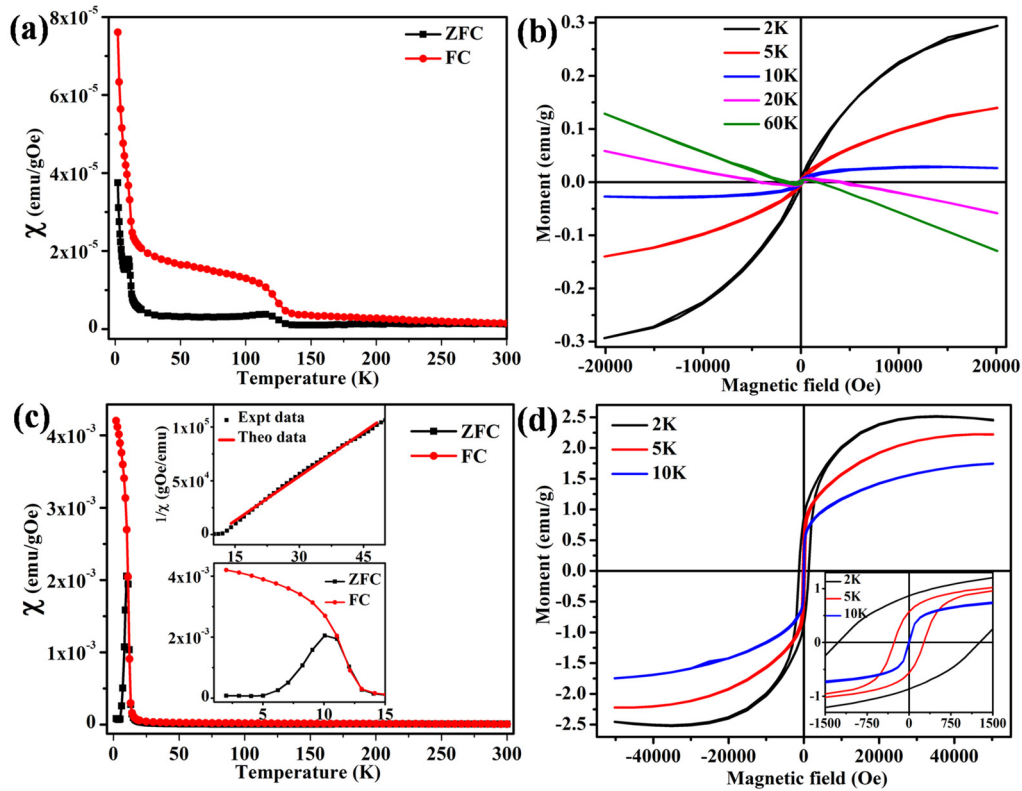


FIG. 7. Magnetization curves. (a) ZFC and FC for sample S6. (b) MH loop for sample S6. (c) ZFC and FC curves for sample S12. Insets show the  $1/\chi$  vs  $T$  curve and enlarged view of the ZFC-FC curves in low-temperature regime. (d) MH loops of sample S12. Inset shows the enlarged view of the coercivity values.

of this layer of  $\text{Co}(\text{OH})_2$  phase grown on the  $\text{MoS}_2$  sheet. The coercivity values extracted from the hysteresis curves at different temperatures are summarized in Table III, from which the highest value of coercivity is obtained as 1271 Oe at temperature 2 K. From the parameters obtained from Rietveld

refinement shown in Table I, it is clear that in the case of the S12 sample, the lattice strain for the as-grown  $\beta\text{-Co}(\text{OH})_2$  phase on  $\text{MoS}_2$  is quite high because of pinning of surface spins along the  $c$  axis, which results in the significant enhancement of coercivity in the thin layer of  $\beta\text{-Co}(\text{OH})_2$  [38–44].

TABLE III. Comparison of coercivity values at different temperatures

Sample	Temperatures (K)	Forward coercivity (Oe)	Reverse coercivity (Oe)	Average coercivity (Oe)
S6	2	156	146	151
	5	190	219	204
	10	233	183	208
	20	272	386	329
	60	195	288	241
S12	2	1266	1277	1271
	5	265	264	264
	10	7	7	7
S18	2	176	173	174
	5	176	173	174
	10	175	170	172
	15	168	171	169
	20	164	162	163
	50	135	133	134
S30	2	162	163	162
	10	137	135	136
	20	112	110	111
	50	60	59	60

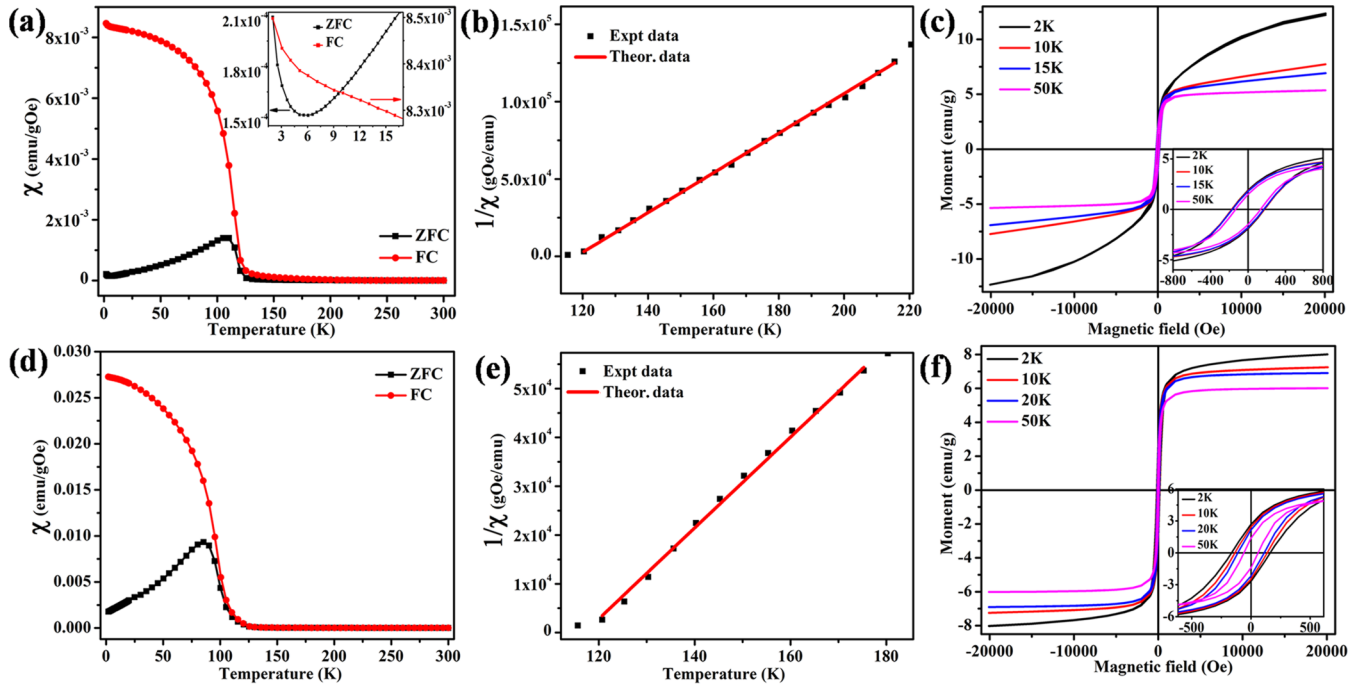


FIG. 8. Magnetization curves. (a) ZFC and FC curves for sample S18. Inset shows the enlarged view of the ZFC-FC curves in low-temperature regime for better view of the paramagnetic tail. (b)  $1/\chi$  vs  $T$  curve for sample S18. (c) MH loops for sample S18 at different temperatures. Inset shows the enlarged view of the coercivity values. (d) ZFC and FC curves for sample S30. (e)  $1/\chi$  vs  $T$  curve for sample S30. (f) MH loops for sample S30 at different temperatures. Inset shows the enlarged view of the coercivity values.

## 2. Magnetic interaction in $\alpha$ -Co(OH)<sub>2</sub>/MoS<sub>2</sub> phase

In the case of the S18 sample, the ZFC curve shows only one peak at 108 K as shown in Fig. 8(a), which is due to the  $\alpha$ -Co(OH)<sub>2</sub> phase. The inset of Fig. 8(a) shows a very small paramagnetic tail in both the FC and ZFC curves, because of which the MH curve does not show perfect saturation at very low temperature, i.e., below 5 K, as shown in Fig. 8(c). With increasing temperature the saturation occurs immediately along with a small amount of coercivity as shown in the inset of Fig. 8(c). This indicates the soft ferromagnetic nature of the sample. We fit a  $1/\chi$  vs  $T$  plot with Curie-Weiss law  $\frac{1}{\chi} = \frac{T-\Theta}{C}$  [Fig. 8(b)] and we get the Curie constants  $\Theta = 117.99$  K and  $C = 7.79 \times 10^{-4}$  emu Kg<sup>-1</sup> Oe<sup>-1</sup> (Table IV). For this sample, using the relation  $N = \frac{N_A M}{M_w}$ , the total Co<sup>2+</sup> ions present per gram of the sample  $N$  is obtained as  $2.09 \times 10^{20}$ . For Co<sup>2+</sup> we have taken the  $g$  value as 2.191 [32]. Using the formulas  $C = \frac{N\mu^2}{3k_B}$ , and  $\mu^2 = g^2\mu_B^2 S(S+1)$ , we get the value of the average spin as  $S = 1.48$ . And using the formula  $M_S = Ng\mu_B(S)$  we have calculated the

saturation magnetization as  $M_S = 6.35$  emu/g Oe, whereas the experimental value obtained from the asymptote of the MH curve as  $T \rightarrow 0$  K is  $M_S = 5.30$  emu/g Oe (Table V). In the case of  $\alpha$ -Co(OH)<sub>2</sub>, there are Co<sup>2+</sup> octahedra along with a number of Co<sup>2+</sup> tetrahedra with the charge balancing anion (in our case it is an acetate ion) [45] along the  $c$  axis and because of some amount of excess water intercalated between two layers of Co(OH)<sub>2</sub>, the effective  $c$  axis is much higher than the  $\beta$ -Co(OH)<sub>2</sub> phase [1,15,45]. And the antiferromagnetic coupling between two interlayer Co<sup>2+</sup> octahedra diminishes largely with a net ferromagnetic order [15]. But because of the large  $c$  axis, the strength of the ordering is not so large compared to the  $\beta$ -Co(OH)<sub>2</sub> phase. In this regard it is to be mentioned that so far ferromagnetic ordering in  $\alpha$ -Co(OH)<sub>2</sub> has not yet been reported because of the metastability of the phase. In fact, the as-grown  $\alpha$ -Co(OH)<sub>2</sub> phase is transformed into a stable  $\beta$ -Co(OH)<sub>2</sub> phase because of the metastability. However, in the present case for higher concentrations of the Co precursor the  $\alpha$ -Co(OH)<sub>2</sub> phase grown on MoS<sub>2</sub> the surface is stable enough to investigate the ferromagnetic ordering with

TABLE IV. Parameters obtained from linear fit to the Curie-Weiss law.

Sample	$\Theta$ (K)		$C$ (emu Kg m <sup>-1</sup> Oe <sup>-1</sup> )	
	Value	Standard error	Value	Standard error
S12	10.34	0.26	$3.63 \times 10^{-4}$	$4.08 \times 10^{-6}$
S18	117.99	2.06	$7.79 \times 10^{-4}$	$2.80 \times 10^{-5}$
S30	116.95	0.99	$1.07 \times 10^{-3}$	$3.02 \times 10^{-5}$

TABLE V. Calculated average spin value and saturation magnetization data.

Sample	Spin value	Saturated magnetization (emu/g Oe)	
		Calculated value	Experimental value
S12	1.17	3.38	2.52
S18	1.48	6.35	5.30
S30	1.49	8.68	7.24

low coercivity and perfect saturation in the hysteresis curves. It is also to be noted that the  $\alpha$ -Co(OH)<sub>2</sub> phase behaves like a soft ferromagnet with very low coercivity up to 100 K.

In the case of the S30 sample we get stable  $\alpha$ -Co(OH)<sub>2</sub> phase and we get a soft ferromagnetic nature similar to sample S18. In the ZFC curve only one peak is at 85.68 K as shown in Fig. 8(d), which is because the  $\alpha$ -Co(OH)<sub>2</sub> phase is observed. There is a bifurcation between the ZFC and FC curves at 116 K which indicates a ferromagnetic ordering down to this temperature. In this case we get saturation of the MH curves in all temperatures (from 2 to 50 K) at a very low applied magnetic field [as shown in Fig. 8(d)] indicating the soft ferromagnetic nature in this sample. After fitting by Curie-Weiss law the same as before we get the Curie constants  $\Theta = 116.95$  K and  $C = 1.07 \times 10^{-3}$  emu Kg<sup>-1</sup> Oe<sup>-1</sup> (Table IV). For this sample, using the relation  $N = \frac{N_A M}{M_w}$ , the total Co<sup>2+</sup> ions present per gram of the sample  $N$  is calculated as  $2.84 \times 10^{20}$ . For Co<sup>2+</sup>, the  $g$  value is taken as 2.191 [32]. Using the expressions  $C = \frac{N\mu^2}{3k_B}$  and  $\mu^2 = g^2\mu_B^2 S(S+1)$  we get the value of average spin as  $S = 1.49$  and we have calculated the saturation magnetization as  $M_S = 8.68$  emu/g Oe whereas the experimental value obtained from asymptote of the MH curve as  $T \rightarrow 0$  K is  $M_S = 7.24$  emu/g Oe is very close to the calculated value (Table V). In the case of the S30 sample, the amount of  $\alpha$ -Co(OH)<sub>2</sub> is much higher than the S18 sample. Because of this reason we get saturation in the MH curves for a lower value of magnetizing field. The coercivity values as

obtained at different temperatures for samples S18 and S30 are summarized in Table III.

#### IV. CONCLUSION

In summary, two different polymorphs of Co(OH)<sub>2</sub> phases are grown on the MoS<sub>2</sub> surface. By tuning the concentration of the cobalt precursor, stable  $\alpha$ -Co(OH)<sub>2</sub> and  $\beta$ -Co(OH)<sub>2</sub> phases are achieved. A high transition temperature along with complete ferromagnetic saturation is observed for  $\alpha$ -Co(OH)<sub>2</sub>/MoS<sub>2</sub> composite due to intercalation of charge balancing anions in the cobalt hydroxide phase, while for the  $\beta$ -Co(OH)<sub>2</sub> phase on MoS<sub>2</sub>, a high amount of coercivity along with ferromagnetic saturation is obtained. The results are explained on the basis of charge transfer from MoS<sub>2</sub> to Co(OH)<sub>2</sub> which is also experimentally verified by calculation of average spin magnetic moment. These materials with very low coercivity can be treated as soft ferromagnetic materials which have potential application as core material in electromagnets.

#### ACKNOWLEDGMENTS

A.D. and S.B. acknowledge Department of Science and Technology (DST)-INSPIRE, New Delhi, for awarding their fellowships. S.K.S. acknowledges DST, New Delhi, Government of India, for financial support of Project No. SR/NM/NS-1089/2011.

- 
- [1] J. R. Neilson, D. E. Morse, B. C. Melot, D. P. Shoemaker, J. A. Kurzman, and R. Seshadri, *Phys. Rev. B* **83**, 094418 (2011).
- [2] P. Hermet, L. Gourrier, J. L. Bantignies, D. Ravot, T. Michel, S. Deabate, P. Boulet, and F. Henn, *Phys. Rev. B* **84**, 235211 (2011).
- [3] J. D. Rall, M. S. Seehra, and E. S. Choi, *Phys. Rev. B* **82**, 184403 (2010).
- [4] S. D. Tiwari and K. P. Rajeev, *Phys. Rev. B* **77**, 224430 (2008).
- [5] M. Fujihala, M. Hagihala, X. G. Zheng, and T. Kawae, *Phys. Rev. B* **82**, 024425 (2010).
- [6] X. H. Liu, W. Liu, W. J. Hu, S. Guo, X. K. Lv, W. B. Cui, X. G. Zhao, and Z. D. Zhang, *Appl. Phys. Lett.* **93**, 202502 (2008).
- [7] P. Shamba, R. Zeng, J. Q. Wang, and S. X. Dou, *J. Appl. Phys.* **107**, 09A919 (2010).
- [8] H. P. Cong, X. C. Ren, H. B. Yao, P. Wang, H. Cölfen, and S. H. Yu, *Adv. Mater.* **24**, 1309 (2012).
- [9] Z. Liu, R. Ma, M. Osada, K. Takada, and T. Sasaki, *J. Am. Chem. Soc.* **127**, 13869 (2005).
- [10] R. Ma, Z. Liu, K. Takada, K. Fukuda, Y. Ebina, Y. Bando, and T. Sasaki, *Inorg. Chem.* **45**, 3964 (2006).
- [11] J. R. Neilson, B. Schwenzer, R. Seshadri, and D. E. Morse, *Inorg. Chem.* **48**, 11017 (2009).
- [12] T. Takada, Y. Bando, M. Kiyama, and H. Miyamoto, *J. Phys. Soc. Jpn.* **21**, 2726 (1966).
- [13] A. Gupta, S. D. Tiwari, and D. Kumar, *Phys. Status Solidi B* **253**, 1795 (2016).
- [14] Z. Wang and M. S. Seehra, *J. Phys.: Condens. Matter.* **29**, 225803 (2017).
- [15] P. Rabu, S. Angelov, P. Legoll, M. Belaiche, and M. Drillon, *Inorg. Chem.* **32**, 2463 (1993).
- [16] S. Bhattacharya, D. Dinda, B. K. Shaw, S. Dutta, and S. K. Saha, *Phys. Rev. B* **93**, 184403 (2016).
- [17] S. Bhattacharya, E. M. Kumar, R. Thapa, and S. K. Saha, *Appl. Phys. Lett.* **110**, 032404 (2017).
- [18] S. Mandal and S. K. Saha, *Appl. Phys. Lett.* **105**, 022402 (2014).
- [19] H. M. Rietveld, *J. Appl. Crystallogr.* **2**, 65 (1969).
- [20] L. Lutterotti, MAUD 2015, version 2.55.
- [21] C. Yan, H. Jiang, T. Zhao, C. Li, J. Ma, and P. S. Lee, *J. Mater. Chem.* **21**, 10482 (2011).
- [22] <http://sdbs.db.aist.go.jp> (National Institute of Advanced Industrial Science and Technology).
- [23] M. Jing, Y. Yang, Y. Zhu, H. Hou, Z. Wu, and X. Ji, *Electrochim. Acta* **141**, 234 (2014).
- [24] S. Xu, D. Li, and P. Wu, *Adv. Funct. Mater.* **25**, 1127 (2015).
- [25] N. Savjani, E. A. Lewis, R. A. D. Patrick, S. J. Haigh, and P. O. Brien, *RSC Adv.* **4**, 35609 (2014).
- [26] J. Rahbani, N. M. Khashab, D. Patra, and M. A. Ghoul, *J. Mater. Chem.* **22**, 16361 (2012).
- [27] C. Lee, H. Yan, L. E. Brus, T. F. Heinz, J. Hone, and S. Ryu, *ACS Nano*, **4**, 2695 (2010).
- [28] T. I. Koranyi, I. Manninger, Z. Paal, O. Marks, and J. R. Gunter, *J. Catal.* **116**, 422 (1989).
- [29] B. J. Tan, K. J. Klabunde, and P. M. A. Sherwood, *J. Am. Chem. Soc.* **113**, 855 (1991).
- [30] A. J. Akhtar, A. Gupta, B. K. Shaw, and S. K. Saha, *Appl. Phys. Lett.* **103**, 242902 (2013).
- [31] A. J. Akhtar, A. Gupta, D. Chakravorty, and S. K. Saha, *AIP Adv.* **3**, 072124 (2013).
- [32] A. S. Maghoub, J. P. J. McCann, L. Eaves, and B. Cockayne, *J. Phys. C: Solid State Phys.* **16**, L49 (1983).

- [33] S. Erdin and M. van Veenendaal, *Phys. Rev. Lett.* **97**, 247202 (2006).
- [34] X. Liu, C. Z. Wang, Y. X. Yao, W. C. Lu, M. Hupalo, M. C. Tringides, and K. M. Ho, *Phys. Rev. B* **83**, 235411 (2011).
- [35] J. D. Hoffman, B. J. Kirby, J. Kwon, G. Fabbris, D. Meyers, J. W. Freeland, I. Martin, O. G. Heinonen, P. Steadman, H. Zhou, C. M. Schlepütz, M. P. M. Dean, S. G. E. te Velthuis, J.-M. Zuo, and A. Bhattacharya, *Phys. Rev. X* **6**, 041038 (2016).
- [36] J. Hoffman, I. C. Tung, B. B. Nelson-Cheeseman, M. Liu, J. W. Freeland, and A. Bhattacharya, *Phys. Rev. B* **88**, 144411 (2013).
- [37] A. T. Lee and M. J. Han, *Phys. Rev. B* **88**, 035126 (2013).
- [38] H. Ohldag, A. Scholl, F. Nolting, E. Arenholz, S. Maat, A. T. Young, M. Carey, and J. Stohr, *Phys. Rev. Lett.* **91**, 017203 (2003).
- [39] J. S. White, M. Bator, Y. Hu, H. Luetkens, J. Stahn, S. Capelli, S. Das, M. Dobeli, T. Lippert, V. K. Malik, J. Martynczuk, A. Wokaun, M. Kenzelmann, C. Niedermayer, and C. W. Schneider, *Phys. Rev. Lett.* **111**, 037201 (2013).
- [40] B. H. Liu and J. Ding, *Appl. Phys. Lett.* **88**, 042506 (2006).
- [41] X. J. Liu, C. Song, F. Zeng, F. Pan, B. He, and W. S. Yan, *J. Appl. Phys.* **103**, 093911 (2008).
- [42] N. Anuniwat, M. Ding, S. J. Poon, S. A. Wolf, and J. Lu, *J. Appl. Phys.* **113**, 043905 (2013).
- [43] Y. C. Wang, J. Ding, J. B. Yi, B. H. Liu, T. Yu, and Z. X. Shen, *Appl. Phys. Lett.* **84**, 2596 (2004).
- [44] J. D. Rall and M. S. Seehra, *J. Phys.: Condens. Matter* **24**, 076002 (2012).
- [45] J. R. Neilson, J. A. Kurzman, R. Seshadri, and D. E. Morse, *Chem. Eur. J.* **16**, 9998 (2010).